Environmental Earth Sciences (2025) 84:31
https://doi.org/10.1007/s12665-024-12010-5

ORIGINAL ARTICLE

Mineralogy and geochemistry of sands from Playa las Golondrinas, Puerto Rico: an approach to establishing a geogenic background

Audrey Allen[1] · Claire L. McLeod[1] · Liannie C. Velázquez Santana[2] · Maddy Zimmerer[1] · Marion L. Lytle[1] · Ethan Krekeler[1] · Will Amick[1] · Jonathan Tegge[1] · Wilnelly Ventura-Valentín[1] · Jordan Vest[1] · Abigale O'Connor[1] · Barry Shaulis[3] · Landon Stitle[1] · Spencer Snell[1] · Mark P. S. Krekeler[1,4]

Received: 13 May 2024 / Accepted: 30 November 2024

Abstract

Sands from the dune, berm, and shore environments at Playa las Golondrinas (18° 30′ 51″ N, 67° 3′ 26″) were investigated to explore how beach sands could be applied as a potential environmental (geogenic) background for the local region. Grain size is dominantly unimodal classifying as fine to medium sand. Hydraulic conductivity values range from 1.07 cm/s (berm) to 1.49 cm/s (shoreface). Sample mineralogy as constrained by X-ray diffraction (XRD) reveals a dominance of quartz and feldspar with minor Mg-calcite, pyroxene, and olivine. Light microscopy and scanning electron microscopy-energy dispersive spectroscopy (SEM–EDS) support XRD data and indicate the presence of oxide-bearing lithic fragments in addition to biologic materials (e.g., corals. forams). Reflective spectra are consistent with XRD and microscopy. Bulk element concentrations determined using inductively coupled plasma—mass spectrometry (ICP-MS) are consistent with derivation from the arc-related rocks of Puerto Rico's interior exhibiting LILE enrichment, Pb-enrichment, and associated Nb–Ta depletion. The majority of the bulk elemental concentrations are below those of average upper continental crust (UCC) values and element co-variation trends (e.g., wt. % Fe_2O_3 vs. As) are interpreted as geogenic in origin. Berm sands are enriched in Fe, Mn, Ni, Cr, V, and As compared to dune and shore samples and this signature is interpreted as being from a wind-driven winnowing effect. The exact form of As (As^{3+} or As^{5+}) remains unconstrained and thus it is unknown if As is mobile in this environment. Reflective spectra, supported by grain size, mineralogy, and bulk chemistry, enables future remote sensing investigations by providing detailed constraints on sand in environmentally sensitive areas. This study therefore provides local context for metal pollution studies across the region.

Introduction

Sand is an important geologic media for understanding the bulk physical and geochemical properties of a given environment and associated tectonic setting (e.g., Pastore et al. 2021; Oglesbee et al. 2020; Garzanti 2019; Lirong et al. 2017; Argyilan et al. 2015; Garzanti et al. 2013; Pettijohn et al. 2012; Dickinson 1985). Studies of sands can establish a background, or geogenic, elemental context which can then be used to assess the potential pollution and environmental contamination throughout a local area of interest (Barnes et al. 2020; Oglesbee et al. 2020; Matsitsi et al. 2019; Jiang et al. 2013). Effective geogenic background materials ideally should be located away from major pollution sources. Beach environments are appropriate areas for geogenic background sampling for local areas of interest because the sediment source is abundant, dune materials may be stable, and materials can be easily visually screened for potential major anthropogenic contaminants (e.g., petroleum spills, macroplastics, and metal debris associated with the marine environment).

In this study, beach sands from Playa las Golondrinas (GOL) in northwestern Puerto Rico (Fig. 1) are investigated within this context to provide an environmental, geogenic, background for future pollution and remote sensing studies

✉ Mark P. S. Krekeler
krekelmp@miamioh.edu

[1] Department of Geology & Environmental Earth Science, Miami University, Oxford, OH 45056, USA

[2] Department of Geological Sciences, University of Colorado Boulder, Boulder, CO 80309, USA

[3] Trace Element and Radiogenic Isotope Laboratory (TRAIL), University of Arkansas, Fayetteville, AR 72701, USA

[4] Department of Mathematical and Physical Sciences, Miami University Hamilton, Hamilton, OH 45056, USA

Published online: 28 December 2024

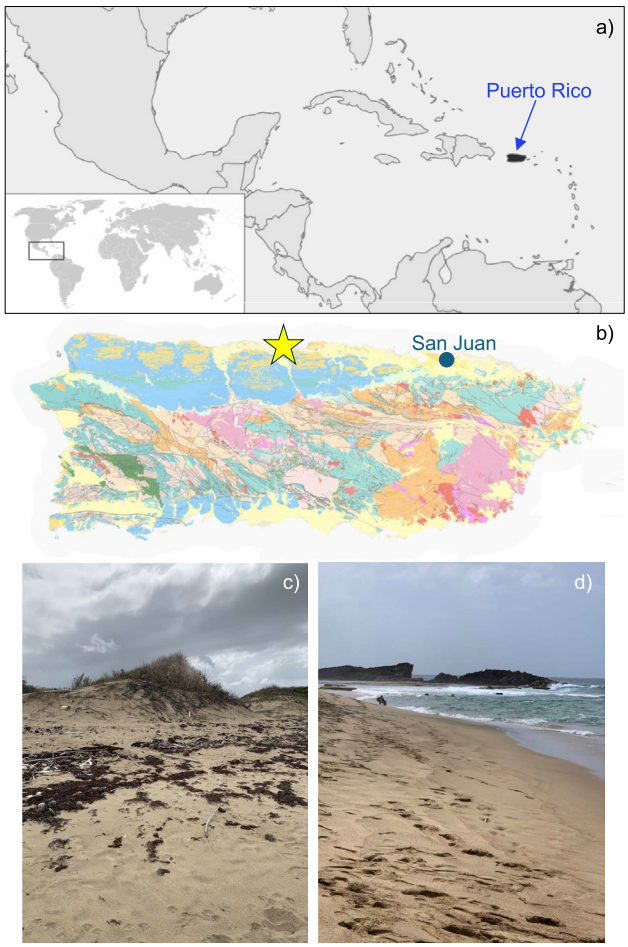

Fig. 1 **a** Location of Puerto Rico within the context of the Caribbean and Latin America. **b** United States Geological Survey (USGS) geological map of Puerto Rico (https://www.usgs.gov/media/images/geologic-map-puerto-rico) showing sample location at Playa las Golondrinas and the capital city of San Juan for reference. See link for explanation. **c** Dune and berm environment of Playa las Golondrinas. **d** Shore environment of Playa las Golondrinas

across the area. Sampled materials from the GOL dune, berm, and shoreface environments are extensively characterized for their physical and chemical properties at the bulk to micrometer scale. This study is the first detailed investigation of sands in Puerto Rico that specifically aims to support future remote sensing and pollution studies.

Geological setting

Puerto Rico is a complex geologic setting that faces numerous geoenvironmental issues including hurricanes (Lin et al. 2020; Kwasinski et al. 2019; Boose et al. 2004; Basnet et al. 1992; Scatena and Larsen 1991), earthquakes, tsunamis (Ventura-Valentín and Brudzinski, 2022; Manaker et al. 2008; Dillon et al. 1999), landslides (Larsen and Torres-Sánchez 1998), and poor water quality (Sánchez-Colón et al. 2022; Sánchez-Colón and Schaffner 2021; Sturm et al. 2012; Rodríguez-Martínez et al. 2006). Puerto Rico is also broadly recognized as an area of environmental need and concern within the context of environmental justice such as access to clean drinking water and remediation (Brown et al. 2018; Lloréns and Santiago 2018; McCaffrey 2018; Wu and Heberling 2013; Epting 2015; Skanavis 1999). Furthermore, generating detailed reflective spectroscopy data to support hyperspectral remote sensing investigations for environmental management and emergency response is an important driver of sand and geomaterial investigations (e.g., Krekeler et al. 2023; Pérez Valentín and Müller 2020; LeBlanc et al. 2016; Tomic et al. 2012; Heggie and Amundson 2009; Heggie and Heggie 2009; Carlson et al. 2007; Ustin et al. 2002).

Playa las Golondrinas (18° 30′ 51″ N, 67° 3′ 26″, Fig. 1) forms the basis of this study and is situated on the northern coast of Puerto Rico. This specific location was selected as it is distant from major pollution sources, urban areas, and agriculture, in addition to having an extensive, well-developed dune system. The local bedrock is the Aymamón Limestone Formation which consists of fine crystalline and fossiliferous white to pale orange limestone (Monroe 1968). The limestone is overlain by slightly fossiliferous pale orange to bright yellow chalk with an estimated maximum thickness of 200 m (Monroe 1968). Winds are dominantly from the east and northeast as estimated from 2000 to 2023 data from San Juan (~ 75 miles to the east) as no direct wind data is available for the sampled GOL site (Iowa State Environmental Mesonet, 2023). Annual temperatures vary from 21° to 32° C for coastal areas and annual precipitation totals are approximately 150 cm for the north coast (USGS, Climate of Puerto Rico, 2023).

Analytical methods

Three sets of 5 samples each of shoreface, berm, and dune were obtained at Playa las Golondrinas. Approximately 1 kg samples were acquired in Ziploc storage bags and were securely shipped.

Grain size characteristics

Grain size distributions were determined using standard 8″ ASTM mechanical brass sieves, with mesh sizes ranging from 38 to 6300 µm, and a Gilson mechanical shaker. Samples were dried in an oven at 60 ºC and 200 g of sand was then used for each sample. Data collected was evaluated in the Gradistat Excel program (Blott and Pye 2001) for analysis and statistical evaluation. Gradistat files are provided in

supplemental materials for reference and include a summary of sample mean, sorting, skewness, kurtosis, and mode.

Hydraulic Conductivity

Falling head permeameter tests were conducted with one sand sample from each sample site. Approximately 170 to 270 g of dry sand was placed into a falling head permeameter followed by 250 mL of tap water. The height of the sand and the head were recorded. After removing the stopper at the base of the falling head permeameter, the time it took the water to fall every 5 mL was recorded to calculate a discharge rate. To determine hydraulic conductivity (K), the height of the sediment was multiplied by the slope of the discharge rate (s) vs. head (cm). After three replicate trials, an average K value was calculated.

Polarized Light Microscopy (PLM)

One thin section from each sampled site (dune, berm, shore) was investigated using a Leica DM2700 P microscope. Criteria of Nesse (2013) were used for mineral identification. Specific samples investigated include GOL Berm 3, GOL Dune 3, and GOL Shore 3. This is the same set of samples which were investigated via hydraulic conductivity.

Powder preparations

Sample splits from all 15 samples were powdered for subsequent analysis via basic powder X-ray diffraction (XRD) and inductively coupled plasma-mass spectrometry (ICP-MS). Samples were prepared using a SPEX 8000 mini-mill using an alumina oxide container. Milling time was 10 min and resulting powders were placed in snap cap plastic vials for temporary storage. Approximately 5 g of material was powdered.

Powder X-Ray diffraction (XRD)

Basic powder X-ray diffraction (XRD) was used to identify major mineral phases with a Bruker D8 Advance ECO X-Ray diffractometer using Cu Kα radiation. Detection limits are estimated at a few wt. %. All sand samples (n = 15) were analyzed from 5° to 65° 2Θ, with a step size of 0.01° 2Θ at 0.5 s/step intervals. Mineral identifications were made using PDF cards, including quartz PDF No. 00–046–1045, calcite PDF No. 00–047–1743, and dolomite No. 00–036–0426. Feldspars were identified including calcian ordered albite PDF No. 00–041-1480, ordered microcline PDF No. 00–019-0926, intermediate microcline PDF No. 00–019-0932, and orthoclase PDF No. 00–031-0966, as well as guidance from Chen (1977). Amphibole was identified by a (011) reflection of ~ 8.50 Å, based on a comparison to several PDF cards and Chen (1977). It is well-recognized that numerous peaks of the feldspar minerals overlap (e.g., Smith 2012; Chen 1977), and some feldspar peaks cannot be identified conclusively; however, PLM data supports the presence of multiple feldspars.

Scanning Electron Microscopy (SEM)

For SEM–EDS investigation, sand from the dune, berm, and shore environments were mounted onto a 10 mm diameter aluminum stub using a carbon adhesive tab. Mounted samples were carbon coated using a Safematic CCU-010 Carbon Coater. A coating thickness of ~ 10 nm of carbon was dispersed within a $7 \times e^{-7}$ Torr vacuum. Data was acquired using a Zeiss 35VP field emission scanning electron microscope (FESEM) under variable pressure (VP) with nitrogen (N_2) as the compensating gas. The FESEM has a backscatter detector (BSD) and an EDS detector (Bruker Quantax). The general sample preparation technique and the Zeiss FESEM instrument have been routinely incorporated into a variety of recent mineralogical and environmental studies (e.g., Allen et al. 2024; Wudke et al. 2024; Flett et al. 2021; O'Shea et al. 2021; Cymes et al. 2020; Klein and Krekeler 2020; Lindeman et al. 2020; Oglesbee et al. 2020; Velázquez Santana et al. 2020; Dietrich et al. 2019, 2018; Burke et al. 2017; Paul et al. 2017). X-ray emission lines used to identify elements observed in the Bruker software include O $K_\alpha = 0.525$ keV; Na $K_\alpha = 1.041$ keV; Mg K = 1.254 keV; Al K = 1.487 keV; Si $K_\alpha = 1.740$ keV, (nominally $K_\beta = 1.837$ keV); S $K_\alpha = 2.309$ keV (nominally $K_\beta = 2.465$ keV); Cl = K_α 2.621 keV; Ca $K_\alpha = 3.690$ and $K_\beta = 4.012$; Fe $K_\alpha = 6.399$ keV and $K_\beta = 7.060$ keV; Ni $K_\alpha = 7.480$ keV and $K_\beta = 8.267$ keV; Cu $K_\alpha = 8.036$ keV and $K_\beta = 8.903$ keV. The ubiquitous occurrence of oxygen in carbonate, silicate, and oxide phases (or adjacent particles); scatter from the aluminum stub and lacey carbon sticky tab and coating; and the substrate, collectively contribute Al, O, and C signal to EDS spectra. The detection limit for EDS is approximately 0.08 wt. % (e.g., Kuisma-Kursula 2000). Sand materials were not pre-washed in deionized water so as not to remove potential pollutant particulate matter or elements of environmental concern. In part, the ubiquitous observation of Na, Cl, Mg, and S is interpreted to originate from evaporated seawater (see supplementary Fig. 1).

Inductively Coupled Plasma—Mass Spectrometry (ICP-MS)

Splits from all 15 sand samples were prepared for bulk elemental analysis by ICP-MS. Sample powder was retrieved from the same powdered sample vial that was analyzed via PXRD. Six standard reference materials (SRMs), chosen to bracket the elemental composition of the sands, were

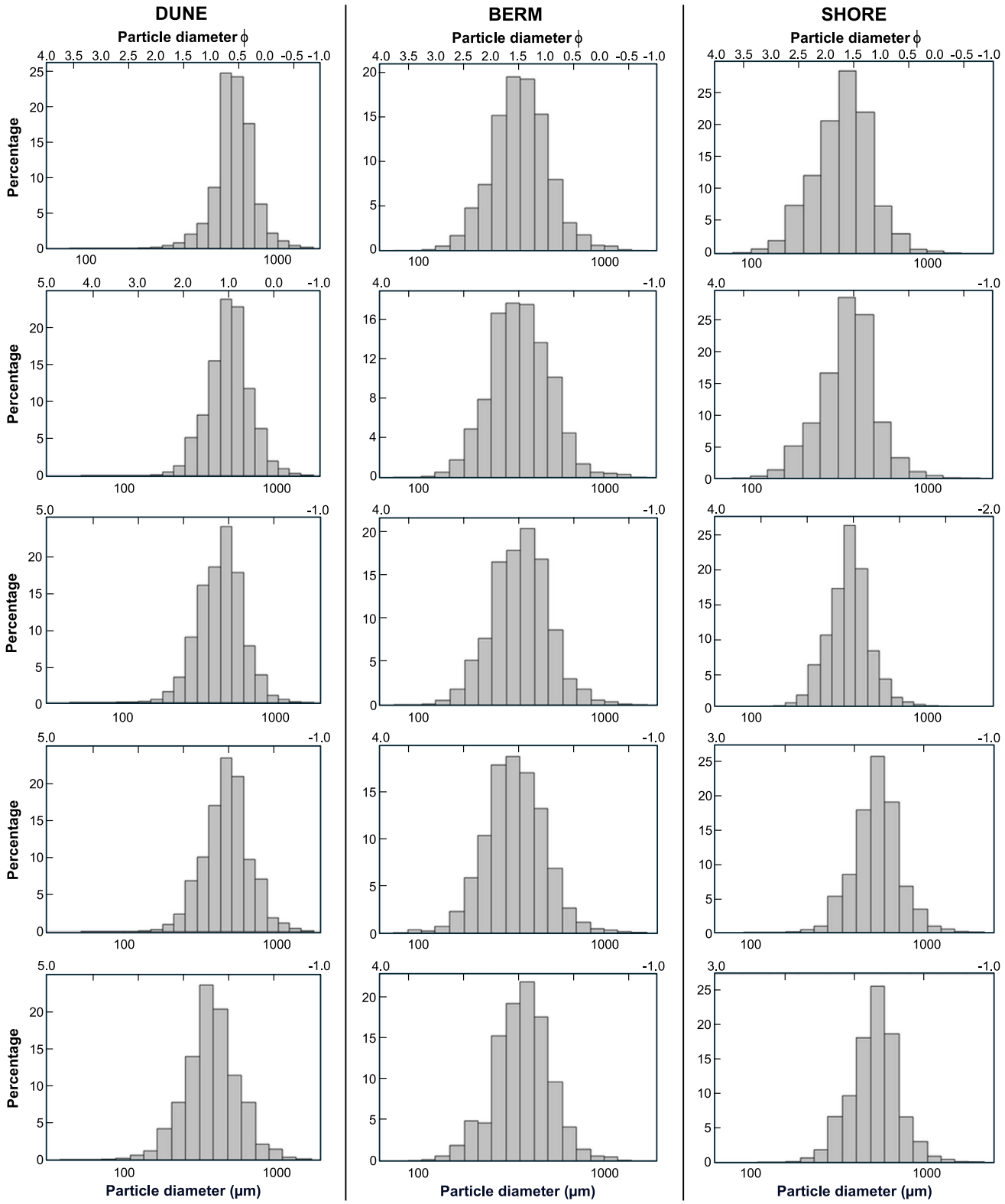

Fig. 2 Histograms showing the dominantly unimodal grain size distribution of sampled sands from the dune, berm, and shoreface environments of Playa las Golondrinas. The X axis for all plots defines particle diameter in micrometers. The Y axis defines the percentage of each standard size classification. Data is provided in supplemental Table 1

Table 1 Bulk elemental concentrations from ICP-MS indicate elevated levels of REE's, Zr, U, and Fe-oxides consistent with the natural. Data for dune, berm, and shore samples are included

	P_2O_5*	TiO_2*	Al_2O_3*	Fe_2O_3*	MgO*	CaO*	MnO*	Na_2O*	Sc	V	Cr	Co	Ni	Cu	Zn	As
GS1 (Shore)	0.05	0.17	11.3	3.4	1.59	0.71	0.04	1.93	5.0	57.0	28.3	3.4	6.1	9.2	36.7	11.3
GS2 (Shore)	0.05	0.16	10.7	3.1	1.54	0.71	0.04	1.95	4.3	53.0	26.4	3.1	5.8	12.4	34.8	10.7
GS3 (Shore)	0.07	0.19	10.7	3.5	1.60	0.72	0.05	1.94	4.7	62.0	27.9	3.5	6.3	9.3	44.7	10.7
GS4 (Shore)	0.05	0.16	11.2	3.0	1.46	0.65	0.04	2.01	4.2	50.6	23.5	3.0	5.4	9.1	35.4	11.2
GS5 (Shore)	0.05	0.14	11.5	3.1	1.44	0.64	0.04	2.01	4.3	49.4	25.0	3.1	5.5	9.9	26.6	11.5
GB1 (Berm)	0.05	0.49	14.3	6.5	2.29	0.86	0.09	1.60	12.0	126.8	95.8	6.5	11.2	12.4	48.2	14.3
GB2 (Berm)	0.04	0.54	14.4	6.2	2.28	0.88	0.10	1.53	11.4	118.3	87.5	6.2	11.2	13.3	45.2	14.4
GB3 (Berm)	0.06	0.48	14.4	6.3	2.28	0.88	0.09	1.52	12.3	124.5	90.7	6.3	11.0	12.8	35.5	14.4
GB4 (Berm)	0.07	0.58	15.3	7.1	2.27	0.86	0.10	1.42	12.5	142.8	89.3	7.1	11.5	12.4	41.5	15.3
GB5 (Berm)	0.06	0.38	14.0	5.5	2.14	0.85	0.08	1.65	10.0	98.9	78.6	5.5	10.3	17.3	46.4	14.0
GD1 (Dune)	0.05	0.28	11.5	4.5	1.49	0.58	0.06	1.90	6.9	80.6	51.0	4.5	8.4	12.0	47.3	11.5
GD2 (Dune)	0.06	0.22	10.6	4.1	1.46	0.60	0.05	1.88	5.7	67.2	33.5	4.1	7.2	11.8	53.8	10.6
GD3 (Dune)	0.05	0.22	9.8	3.6	1.48	0.64	0.05	1.90	5.9	56.6	27.8	3.6	6.1	10.2	34.2	9.8
GD4 (Dune)	0.05	0.18	10.0	3.6	1.41	0.61	0.05	1.84	5.9	58.0	30.7	3.6	6.3	9.5	30.8	10.0
GD5 (Dune)	0.06	0.22	10.5	4.4	1.46	0.59	0.05	1.89	6.5	75.1	42.4	4.4	8.2	11.7	43.8	10.5
AVG.	0.05	0.29	12.02	4.52	1.75	0.72	0.06	1.80	7.44	81.38	50.55	4.52	8.02	11.57	40.33	12.02
MIN.	0.04	0.14	9.77	3.02	1.41	0.58	0.04	1.42	4.18	49.35	23.46	3.02	5.37	9.10	26.63	9.77
MAX.	0.07	0.58	15.30	7.09	2.29	0.88	0.10	2.01	12.45	142.78	95.84	7.09	11.52	17.34	53.75	15.30
ST.DEV.	0.01	0.16	1.88	1.41	0.37	0.12	0.02	0.20	3.21	32.19	28.74	1.41	2.38	2.16	7.51	1.88

	Rb	Sr	Y	Zr	Nb	Cs	Ba	La	Ce	Pr	Nd	Sm	Eu	Gd	Tb	Dy
GS1 (Shore)	26.8	602.8	6.0	10.5	1.1	0.4	504.0	5.6	10.1	1.4	5.4	1.2	0.5	1.2	0.1	0.9
GS2 (Shore)	27.4	601.0	5.4	10.3	1.0	0.3	548.2	5.4	9.2	1.2	4.9	1.0	0.4	1.0	0.1	0.9
GS3 (Shore)	27.5	608.3	5.8	10.6	1.2	0.3	541.9	5.0	8.9	1.2	5.0	1.1	0.4	1.1	0.1	1.0
GS4 (Shore)	28.8	553.1	5.5	10.7	1.6	0.3	572.2	5.6	10.3	1.3	5.1	1.0	0.4	1.0	0.1	0.9
GS5 (Shore)	27.2	549.3	5.2	10.4	0.8	0.3	521.8	5.8	9.4	1.2	4.6	1.0	0.4	1.0	0.1	0.8
GB1 (Berm)	21.0	661.7	13.3	16.2	3.8	0.3	391.4	11.9	23.9	3.2	13.0	2.8	0.8	2.6	0.4	2.3
GB2 (Berm)	20.5	688.7	13.8	14.9	4.8	0.3	400.2	11.3	23.4	3.1	12.8	2.8	0.8	2.6	0.4	2.4
GB3 (Berm)	19.7	687.3	13.5	15.4	3.9	0.3	374.9	12.3	24.8	3.4	13.4	2.9	0.8	2.6	0.4	2.4
GB4 (Berm)	19.9	672.4	16.5	15.6	4.9	0.3	360.7	14.7	31.7	4.3	16.8	3.4	0.9	3.2	0.4	2.9
GB5 (Berm)	21.9	660.8	11.0	13.4	2.9	0.3	409.9	11.0	20.3	2.6	10.5	2.2	0.7	2.1	0.3	1.8
GD1 (Dune)	27.2	532.6	7.6	14.1	1.9	0.4	533.6	7.0	13.1	1.7	7.1	1.5	0.5	1.5	0.2	1.3
GD2 (Dune)	26.2	534.0	7.1	11.6	1.6	0.3	514.7	6.4	11.8	1.6	6.4	1.4	0.5	1.3	0.2	1.2
GD3 (Dune)	26.1	535.6	6.4	11.1	1.5	0.3	497.3	5.8	10.5	1.4	5.6	1.2	0.4	1.1	0.1	1.0
GD4 (Dune)	26.1	536.2	6.4	11.3	1.2	0.4	497.2	9.6	14.9	1.7	6.4	1.2	0.5	1.2	0.1	1.0
GD5 (Dune)	25.7	514.8	6.4	10.8	1.5	0.4	476.0	9.1	11.9	1.4	5.7	1.2	0.5	1.1	0.1	1.0
AVG.	24.8	595.9	8.7	12.5	2.2	0.3	476.3	8.4	15.6	2.1	8.2	1.7	0.6	1.6	0.2	1.5
MIN.	19.7	514.8	5.2	10.3	0.8	0.3	360.7	5.0	8.9	1.2	4.6	1.0	0.4	1.0	0.1	0.8
MAX.	28.8	688.7	16.5	16.2	4.9	0.4	572.2	14.7	31.7	4.3	16.8	3.4	0.9	3.2	0.4	2.9
ST.DEV.	3.2	63.9	3.8	2.2	1.4	0.0	69.8	3.2	7.3	1.0	4.0	0.8	0.2	0.8	0.1	0.7

Table 1 (continued)

	Ho	Er	Tm	Yb	Lu	Hf	Ta	Pb	Th	U
GS1 (Shore)	0.1	0.5	0.0	0.5	0.1	0.4	0.1	7.1	0.8	0.4
GS2 (Shore)	0.1	0.5	0.0	0.5	0.1	0.4	0.1	7.3	0.8	0.4
GS3 (Shore)	0.1	0.5	0.0	0.5	0.1	0.4	1.5	7.0	0.8	0.4
GS4 (Shore)	0.1	0.5	0.0	0.5	0.0	0.4	0.1	6.4	0.8	0.4
GS5 (Shore)	0.1	0.4	0.0	0.4	0.0	0.4	0.1	12.1	1.2	0.3
GB1 (Berm)	0.4	1.3	0.2	1.4	0.3	0.7	0.4	8.7	1.9	1.1
GB2 (Berm)	0.4	1.4	0.2	1.4	0.2	0.8	0.5	8.7	2.3	1.1
GB3 (Berm)	0.4	1.3	0.1	1.2	0.2	0.7	0.4	9.0	1.7	1.1
GB4 (Berm)	0.5	1.6	0.2	1.6	0.2	0.8	0.5	9.2	2.0	1.2
GB5 (Berm)	0.3	1.1	0.1	1.0	0.1	0.6	0.3	8.0	1.5	0.9
GD1 (Dune)	0.2	0.7	0.0	0.7	0.1	0.5	0.2	7.6	1.2	0.6
GD2 (Dune)	0.2	0.7	0.0	0.6	0.0	0.5	0.1	6.9	0.8	0.5
GD3 (Dune)	0.2	0.6	0.0	0.6	0.1	0.4	0.2	7.7	0.8	0.4
GD4 (Dune)	0.2	0.6	0.0	0.6	0.0	0.4	0.1	6.8	1.1	0.4
GD5 (Dune)	0.1	0.6	0.0	0.5	0.0	0.4	0.1	6.8	0.6	0.3
AVG.	0.2	0.8	0.0	0.8	0.1	0.5	0.3	8.0	1.2	0.6
MIN.	0.1	0.4	0.0	0.4	0.0	0.4	0.1	6.4	0.6	0.3
MAX.	0.5	1.6	0.2	1.6	0.3	0.8	1.5	12.1	2.3	1.2
ST.DEV.	0.1	0.4	0.1	0.4	0.1	0.1	0.4	1.4	0.5	0.3

included in the sample batch to monitor and ensure data quality and accuracy. The SRMs chosen were BHVO-2 (USGS; Hawaiian basalt), BCR-2 (USGS; Columbia River basalt), DNC-1 (USGS; North Carolina diabase), GSP-2 (USGS; Colorado Silver Plume granodiorite, SCo-1 (USGS; Cody shale), and AGV-2 (USGS; Oregon Guano Valley andesite). Approximately 0.0500 g ± 0.0050 g of each powdered SRM and unknown sample was weighed and put into an acid cleaned and labeled Teflon Savillex beaker. Once all samples were weighed, the bulk digestion process took five days, using distilled, ultra-clean acids and ultra-pure water in all steps. Powders were digested by HNO_3:HF acid attack following the methods of Anderson et al., (2021), Lytle et al., (2012), and Kelley et al., (2003). See supplemental materials for the detailed methods.

Samples, standards, and total procedural blanks were analyzed for their elemental concentrations via a Thermo iCap Inductively Coupled Plasma Mass Spectrometry (ICP-MS) coupled to a CETAC ASX-560 autosampler at the Trace Element and Radiogenic Isotope Laboratory (TRAIL) at the University of Arkansas. The ICP-MS was calibrated by using two multi-element standards (68 A, High Purity Solutions; 71B Inorganic Ventures). Calibration curve measurements were made using a series of seven dilutions with concentrations ranging from 1 µg/kg to 1000 µg/kg. The above analytical approach has previously been used in Wudke et al., (2024) and Flett et al., (2021).

Reflective Spectroscopy

The experimental substrates for reflective spectra measurements were plastic Petri dishes painted with flat black spray paint. Approximately 5 g of sand split from each bulk sample (n = 15) were dried using the methods described earlier (see: grain size characteristics). Spectra were acquired using a contact probe to acquire the most uniform or clean signal using an ASD FieldSpec 4 Hi-Res spectroradiometer. This instrument has a spectral range of 350 to 2500 nm and spectral resolutions of 3 nm at 700 nm, and 8 nm at 1400 nm and 2100 nm respectively for the visible (VIS), near infrared (NIR), and shortwave infrared (SWIR). This spectroradiometer is equipped with a modular silicon array and a Peltier-cooled InGaAs detector spectrometer platform. The instrument is equipped with a post-dispersive system for extremely low stray light which is at < 0.02% for 350 to 1000 nm and < 0.1% for 1000 to 2500 nm. Low noise equivalent delta radiance (NeDL) values are 1.1×10^{-9} W/cm^2/sr/nm at 700 nm for UV/VNIR, 2.8×10^{-9} W/cm^2/sr/nm at 1400 nm for NIR and 5.6×10^{-8} W/cm^2/sr/nm at 2100 nm. Well established and accepted reflective spectroscopy literature and the USGS spectral library was used to determine bond assignments for spectra (Curran et al. 1990; Cloutis 1989; Hunt 1977; Hunt et al. 1973; Hunt and Logan 1972; Hunt et al. 1971a, b). Assignments were informed by mineral identifications based on PLM and PXRD data.

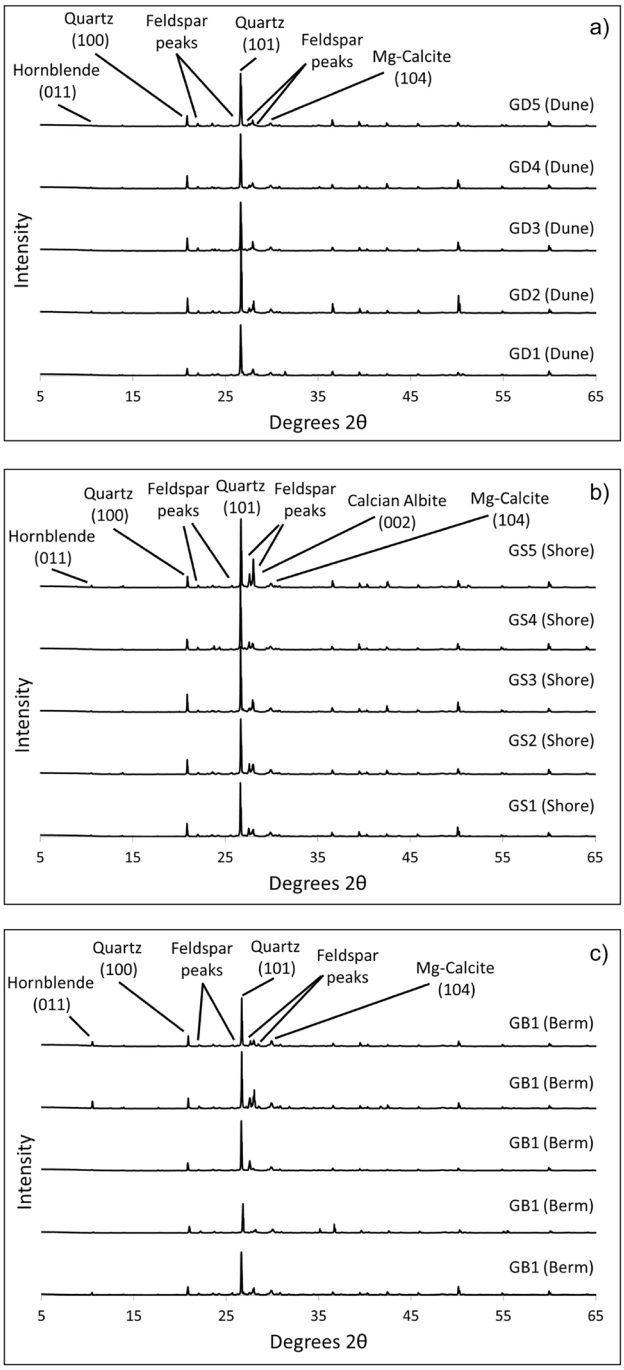

Fig. 3 Powder X-ray diffraction (XRD) patterns of sampled sands from the dune, berm, and shore environments of Playa las Golondrinas. Quartz, feldspars, hornblende, and Mg-calcite are the primary minerals present with their major lines labeled. Labels for minor peaks at (or near) detection limits for calcite, pyroxene and olivine are omitted for clarity. Owing to the complexity of the feldspar diffraction patterns and peak overlap only their major lines are labeled

The instrument and similar methods as described above have been used in numerous previous investigations (e.g., Curtis et al. 2023; Krekeler et al. 2023; Barnes et al. 2020, Brum et al. 2020; Oglesbee et al. 2020; Burke et al. 2019; Allen and Krekeler, 2010; Krekeler and Allen 2008).

Results

Grain size characteristics

The grain size for all samples (n = 15) is unimodal except for one sample (Berm #5) which is bimodal (Fig. 2). The mode for both dune and shore sands is 462.5 µm. The mode for berm sands is slightly more variable being 327.5 µm (Berm 1, 2, 4), 390 µm (Berm 3), and 390 µm and 196 µm (Berm 5). Cumulative plots for each sample are provided in the Supplemental Materials Table 1, and uniformity coefficients derived from these plots average 0.60 for dune, 0.64 for berm, and 0.69 for shoreface.

Hydraulic Conductivity

Hydraulic conductivity (K) values were determined for one sample of each of the dune sand, berm sand, and shoreface sand (and the sample analysis replicated 3 times). Average values vary amongst the sample types and are 1.16 cm/s for dune sands, 1.07 cm/s for berm sands, and 1.49 cm/s for shoreface sands. The values of GOL samples fall within the range of well-sorted sands; however, their relatively high K values are also consistent with fine gravels (Fetter 2018). This is in part attributed to the high degree of sorting, the intragranular porosity, and the irregular grain shapes of the fossil grains.

Powder X-ray diffraction (XRD)

Powder XRD results are shown in Fig. 3. Results indicate that quartz is the dominant mineral; however, several other peaks are identified. The commonly observed major peaks of quartz are $d_{(101)} = 3.34$ Å and $d_{(101)} = 4.26$ Å and commensurate less intense peaks are often observed. Calcian-ordered albite is indicated by a major peak at $d_{(002)} = \sim 3.18$ Å. Other peaks present at ~ 3.83 Å, 3.70 Å, 3.47 Å, 3.31 Å, and 3.24 Å are consistent with ordered microcline, intermediate microcline, and orthoclase. The exact identification of mixed feldspar species is challenging via XRD owing to the numerous potential peak overlaps and the presence of numerous feldspar species. A peak for amphibole was observed in some samples interpreted as the $d_{(020)}$ of ~ 8.50 to 8.40 Å. This is consistent with hornblende observed in PLM. The major peak and value that is observed for calcite is $d_{(104)} = 3.035$ Å. However, peaks for calcite were near detection limits. Minor peaks observed at ~ 2.99 to 3.01 Å are consistent with pyroxene minerals and Mg-calcite. Minor peaks near detection

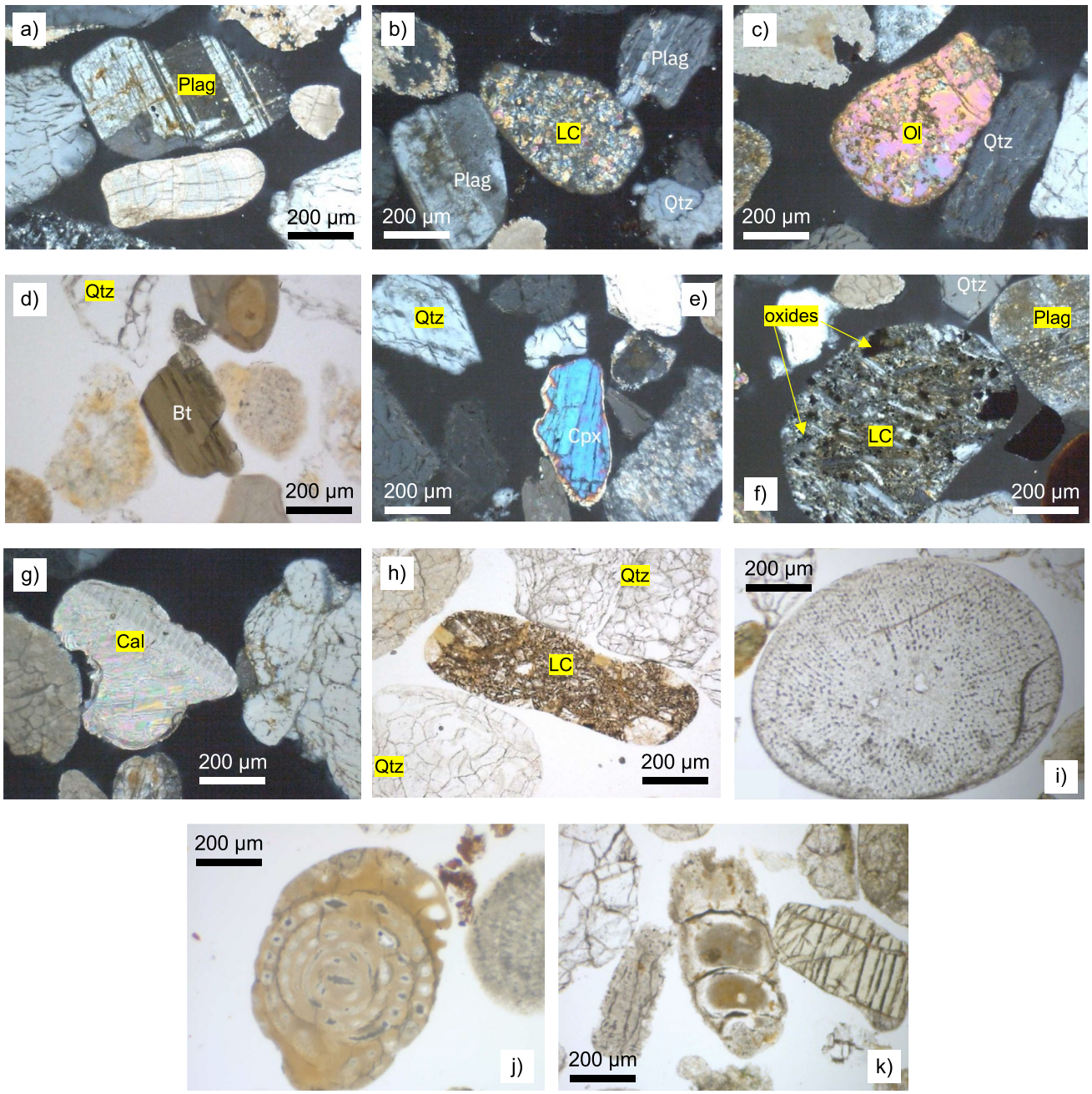

Fig. 4 Polarized light microscopy (PLM) images for samples dune (**a**-**c**), berm (**d**-**f**), and shore (**g**,**h**) sands. In panels i-k, representative fossil fragments are shown: **i**) echinoderm, **j**) and **k**) fragmented forams. *Plag* plagioclase feldspar, *Qtz* quartz; *LC* lithic clast, *Olv* olivine; *Bt* biotite; *Cpx* clinopyroxene; *Cal* calcite

limits observed at ~ 2.83 Å to 2.79 Å are consistent with olivine (e.g., Chen 1977).

Polarized Light Microscopy (PLM)

PLM data indicates that the major and minor mineralogy of sands from the dune, berm, and shore are similar (Fig. 4a-h). Major minerals include quartz (up to 70%), plagioclase feldspar (up to 10%), minor olivine, pyroxene, and lithic clasts (total < 15%), fossil fragments (~ 15%), and less common grains of calcite, amphibole, oxides, and biotite (< 1%). Notably, lithic clasts often contain 5–10% oxides (Fig. 4f). Mineral grain sizes varied, but average diameters were generally 200–1000 µm throughout all samples and were consistent with bulk grain size analysis.

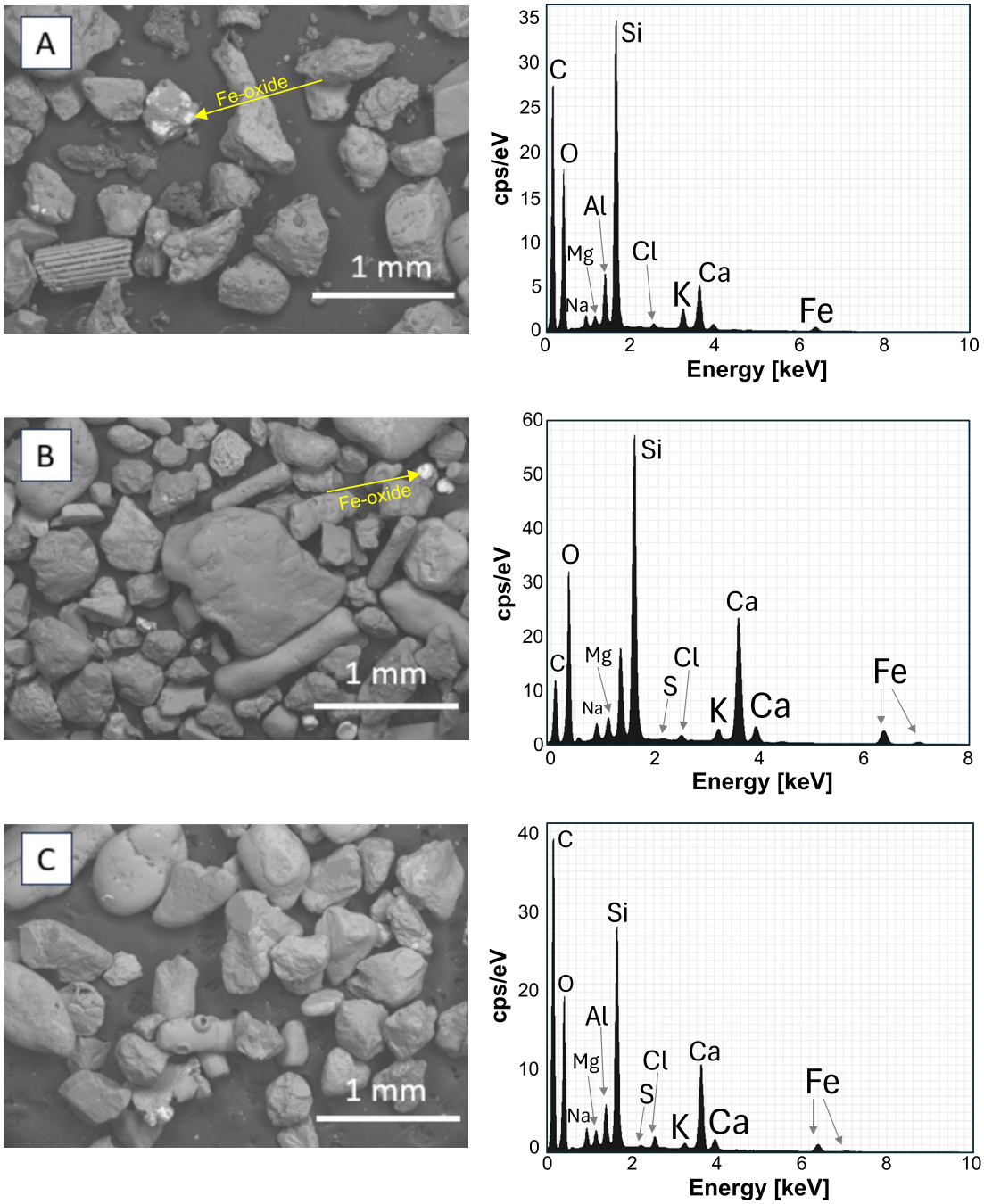

Fig. 5 Representative SEM images with paired EDS spectra from the overall area. Major and minor spectra are labeled and are consistent with PLM and XRD observations

Microscopic fossils and fossil fragments were commonly observed (Fig. 4i-k). While specific species cannot reliably be identified owing to abrasion, general fossil types can be distinguished (e.g., AAPG 1978). Echinoderm plates are common and found in both the dune and berm sands. Foraminifera are common in all sand types. Mollusk fragments are also observed, with some identified as gastropods owing to their spiral morphology shape and multi-chamber structure (e.g., Strekeisen 2020). Shell fragments are variable in size from ~ 300 to 500 µm with altered or fragmented structures. A majority of the intragranular porosity is attributed to these fossils, with estimated average intragranular porosities of ~ 30% (typical diameters: 10–25 µm), ~ 25% (typical diameters: 7–25 µm), and ~ 25% (typical diameters: 5–50 µm) for the dune, berm, and shore samples respectively.

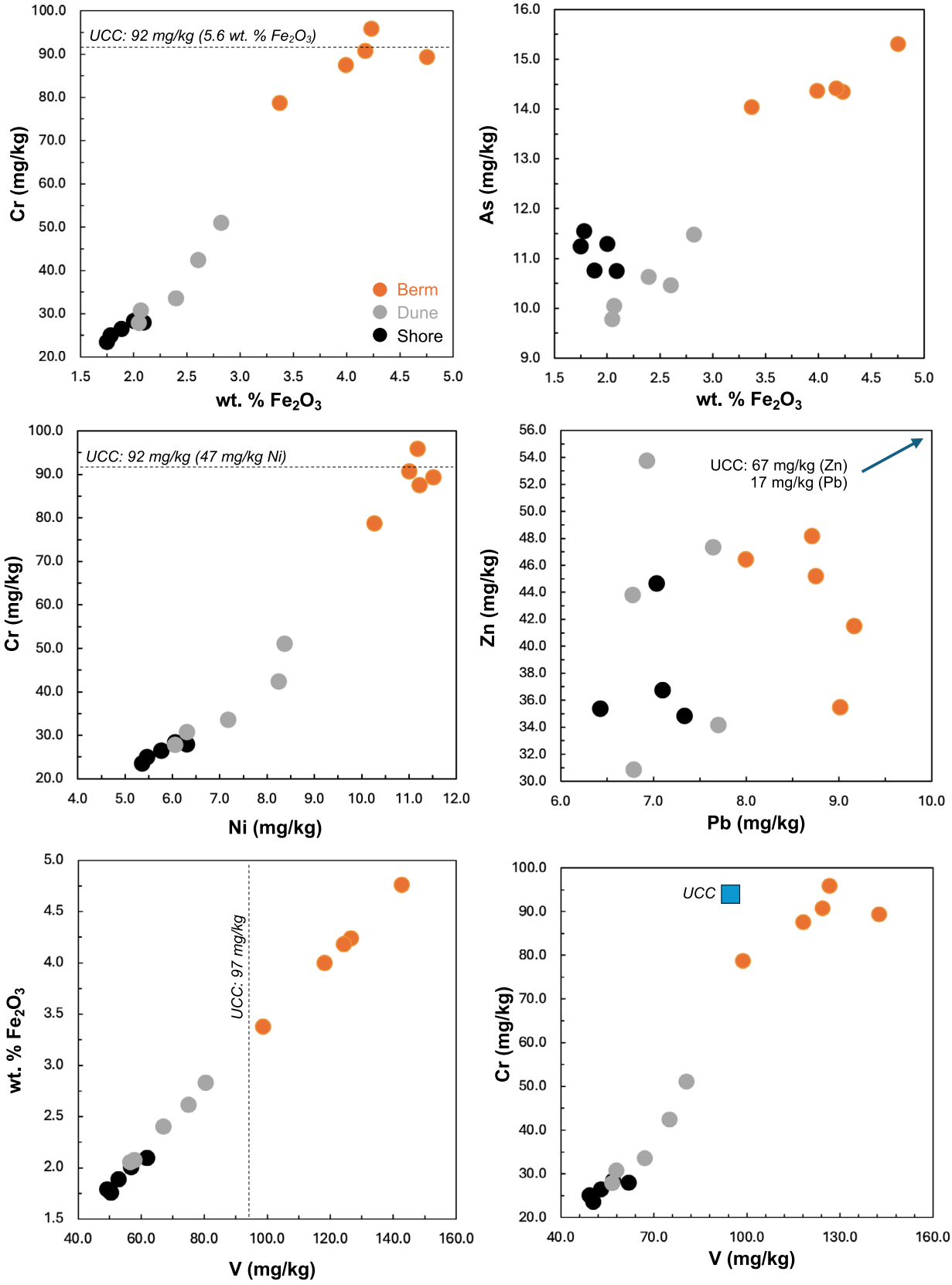

Fig. 6 Select element vs. element graphs for sampled dune, berm, and shore sands. Consistently, berm samples exhibit higher wt. % Fe_2O_3 contents accompanied by higher concentrations of Cr, As, Ni, and V (mg/kg). See text for discussion

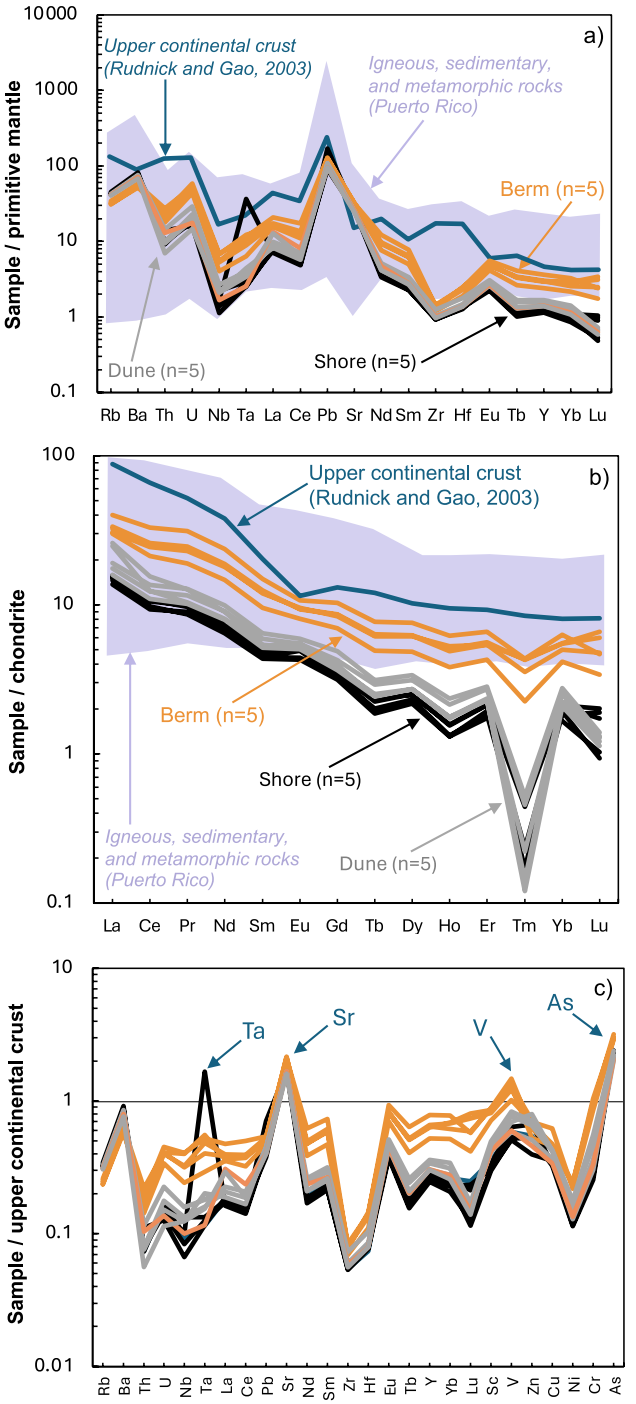

Fig. 7 **a** Primitive mantle-normalized spidergram (values after Sun and McDonough 1989) for sampled Playa las Golondrinas sands, upper continental crust (after Rudnick and Gao 2003), and igneous, sedimentary, and metamorphic rocks from Puerto Rico (database in Hu et al. 2022). **b** Chondrite-normalized rare earth element (REE) profiles of sampled Playa las Golondrinas sands, upper continental crust, and the Puerto Rico database of Hu et al. (2022). Chondrite normalization values after Nakamura (1974). **c** extended upper continental crust-normalized spidergram to include transition metals V, Zn, Cu, Ni, Cr, and As. See text for further discussion

Scanning Electron Microscopy (SEM)

SEM observations of sands indicate a wide range of grain shapes to be present with ~ 85% being equant, ~ 10% being platy to elongated blocky, and ~ 5% being rod-like (Fig. 5a-c). Grains are dominantly subangular and irregular in shape. Equant grains are primarily quartz and feldspar minerals, while the observed rod-like grains are primarily biologic (e.g., rounded coral). Minor platy to blocky grains are associated with olivine and pyroxene minerals. The accompanying EDS spectra of these sands is consistent with XRD and PLM data. Given the marine coastal setting, there is likely some contribution to the EDS spectra of Na, Cl, S, and Mg from seawater. SEM–EDS mapping of an example sand sample shows an uneven distribution of Na and Cl on multiple grain types (supplementary Fig. 1).

Inductively Coupled Plasma Mass Spectrometry (ICP-MS)

ICP-MS data is provided in Table 1. Select element-element relationships between the GOL sands are summarized in Fig. 6. Berm sands are consistently higher in their absolute abundances of wt. % Fe_2O_3, Cr, Ni, V, and As relative to the dune and shoreface sands. These elements show strong positive inter-element correlations (as shown in Fig. 6a-c,e,f). This is consistent with the presence of Fe-oxides into which Cr, Ni, V, and As readily partition, all of which are siderophile. Within the context of elements that can be of environmental concern, Zn and Pb are shown in Fig. 6d with Pb abundances slightly higher (a few mg/kg) in the berm samples. Zinc abundances are similar within (and between) all sampled sands: 27–54 mg/kg. Berm sands consistently exhibit ~ 2–3 mg/kg higher As contents relative to dune and shoreface sands (Fig. 6d). Pearson correlation coefficients are summarized in supplementary Table 2 with positive and negative correlations attributed to the major and minor mineral phases identified and the minor presence of fossil materials. Additional element-element relationships are summarized in supplementary Fig. 2 and are consistent with the observed sample mineralogy.

To evaluate sampled sands as a potential geogenic background for Puerto Rico, the elemental abundances of sampled sands are considered within the context of several of Earth's geochemical reservoirs in Fig. 7a. Sampled sands are shown normalized to the primitive mantle (Sun and McDonough 1989). All sands exhibit very similar normalized profiles with relative enrichment in the large ion lithophile elements (LILEs, e.g., Rb, Ba, Th), a Nb–Ta depletion, and positive Pb anomaly. This geochemical profile is in part similar to that exhibited by the geological record of Puerto Rico which is also shown in Fig. 7a. This geochemical similarity is consistent with the tectonomagmatic

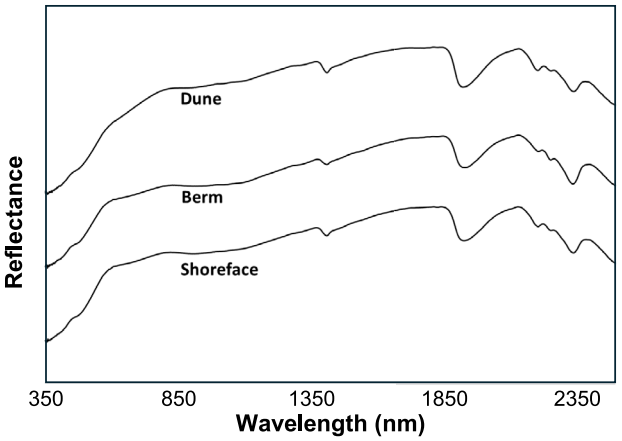

Fig. 8 Representative reflective spectra for dune, berm and shore sands showing relatively uniform absorption features among sample types

history of the region which has been characterized by convergent margin tectonics and associated subduction-related processes since the Cretaceous (e.g., Ramos and Mann 2023; Hu et al. 2022; García-Casco et al. 2008). As shown, within the sampled GOL sands, the berm samples are consistently relatively enriched in most trace elements compared to the dune and shoreface sand samples. Also shown on Fig. 7a is the primitive mantle-normalized trace element profile of Earth's upper continental crust (UCC) reservoir (Rudnick and Gao 2003). Compared to this geochemical reservoir, the GOL sands are relatively depleted in most of the trace elements shown, some by an order of magnitude. In Fig. 7b, the same datasets are shown normalized to a chondritic reservoir to evaluate rare earth element (REE) contents. As shown, all sampled GOL sands are depleted in REEs compared to Earth's UCC and the Puerto Rican geological database, particularly with respect to the middle and heavy rare earth elements (Hu et al. 2022). As a sample suite, all GOL sands are relatively LREE-enriched with La_N/Gd_N from 3.6 to 6.6, similar to that of the UCC (La_N/Gd_N: 6.7; Rudnick and Gao 2003, where "$_N$" denotes the normalized value). Berm sands are relatively enriched in all REEs compared to the dune and shore sands. To illustrate the GOL sands depleted nature compared to the UCC reservoir, Fig. 7c shows an extended trace element spidergram and includes V, Zn, Cu, Ni, Cr and As. The GOL sands are depleted in all elements with the following exceptions: Arsenic (As) in all samples is higher than UCC (As_N from 2.0 to 3.2 with absolute abundances up to 15.3 mg/kg); V in the berm sands is slightly enriched (V_N up to 1.5); Sr is enriched in all samples (Sr_N: 1.6–2.2); and one shore sample exhibits an anomalous positive Ta anomaly (Ta_N: 1.7).

Reflective spectroscopy

Reflective spectra of dune, berm, and shoreface sands are similar with absorption features at ~ 470 nm (Fe^{3+}, Hunt 1977), ~ 1400–1415 nm (OH, H_2O, Hunt, et al. 1971a, b; Curran 1989), a strong feature at ~ 1930 nm (H_2O and OH, Curran 1989), ~ 2210 nm (Al–OH groups, Hunt et al. 1973) small features at 2260 nm (OH), and a strong absorption feature at ~ 2350 nm (carbonate, Hunt 1977). These characteristics are summarized in Fig. 8. Generally, the NIR region of spectra of the dune sand is ~ 5% more reflective than shoreface sands. The shoreface sands are in turn ~ 5% more reflective than berm sands. In the VIS and SWIR, spectra functionally overlap and would likely not be statistically differentiated.

Discussion

Geogenic background

Detailed investigations of sands and other geologic materials (e.g., soils) have the potential to improve understanding of a region's geochemical environmental background and help evaluate the relative contributions from geogenic and/or anthropogenic sources (e.g., Vandeuren et al. 2023; González-Guzmán et al. 2022; Papotto et al., 2022; Oglesbee et al. 2020; Barnes et al. 2020; Matsitsi et al. 2019; Dung et al. 2013; Jiang et al. 2013). A main contribution of this study is the establishment of elemental concentrations in sand media within the context of a geogenic background. It is anticipated that the establishment of this geochemical reference frame will help support future pollution studies, particularly for the coastal and urbanized regions of the island (Pérez-Alvelo et al. 2021; Wu et al., 2013; Apeti et al. 2012).

In 1957, the United States Geological Survey (USGS) reported findings from a reconnaissance study of Puerto Rico beach sands across the island. This work was conducted to first identify "economic heavy minerals" and to subsequently locate their source rocks on the island. The most abundant heavy mineral identified was magnetite (often associated with ilmenite) and was reported to be present in all shore environments. In particular, sands in southern coastal regions were reported to have up to 20% magnetite (USGS 1957). A subsequent study by Meinecke (1972) characterized 24 beach sand samples from across the eastern, northern, and western coastal areas of Puerto Rico. This study reported a dominance of quartz, plagioclase as the major feldspar, and frequent calcareous shells (fragmented). Magnetite, ilmenite, and amphibole (often hornblende) were also reported as common with 75% of

the studied sands also reported to contain staurolite and rutile.

The strong linear correlations of siderophile elements (e.g., Mn, V, Cr, Ni, As) with total Fe_2O_3 in all the GOL sand samples are interpreted as geogenic in origin and are consistent with the presence of Fe-oxides (e.g., magnetite; Fig. 6, supplementary Table 2). If variable anthropogenic sources were introduced into the beach sediment from vehicles and/or atmospheric deposition, extensive scatter would be expected. Similarly, if multiple geogenic sources were contributing to the beach environments at GOL, variable mineralogies and inconsistent co-variation of associated chemistries would also be expected. This is not observed (see Fig. 6). Based on the compositional similarity to the igneous, sedimentary, and metamorphic rock record of Puerto Rico (Fig. 7a-b), the presence of minerals associated with such lithologies (e.g., olivine, biotite, quartz), and the presence of shell fragments, local terrigenous and marine sources are inferred.

The concentrations of Ni (up to ~ 11 mg/kg) and Cr (up to ~ 90 mg/kg), which have the potential to be pollutant metals, are interpreted here as representative of the natural geogenic background. All Ni is below that of average UCC with Cr below (or at) UCC values (see Fig. 7c). As noted earlier, Ni and Cr are interpreted as being associated with Fe-oxides but may also occur in olivine and pyroxene (e.g., Barnes et al. 2023; Jollands et al. 2023; Schoneveld et al. 2020). From PLM observations, olivine and pyroxene are present at < 5 wt. % and are therefore interpreted as contributing only minor amounts of Ni and Cr to the bulk sand compositions. Concentrations of other common potential metal pollutants in the environment include Cu, Pb, and Zn. For the sampled GOL sands, the absolute concentration of these elements is interpreted to be representative of the natural, geogenic background. This is consistent with the fact that no discrete Cu, Pb, or Zn-bearing mineral or anthropogenic phases (e.g., brass, lead metal) were observed via PLM or SEM.

In the GOL sands, As is present at concentrations approximately 2 to 3 times higher than UCC values (Fig. 7c) and strongly correlates with total wt. % Fe_2O_3 (Fig. 7b). This correlation is consistent with the presence of Fe-oxides (e.g., magnetite). In addition, other trace elements which are known to be highly compatible in Fe-oxides are also consistently present at higher concentrations in all berm samples (e.g., Mn, V, Cr; Table 1). The association of Fe_2O_3 and As is well-recognized due to As exhibiting solid solution in Fe-oxides, or being present as inclusions in Fe-oxides (e.g., Mamindy-Pajany et al. 2009; Giménez et al. 2007; Lakshmipathiraj et al. 2006) and Fe-sulfides (e.g., Qiu et al. 2017; Mango and Ryan 2015; Kolker and Nordstrom 2001).

The absolute concentration of As and its association with wt. % Fe_2O_3 is a potentially important constraint in understanding As cycling in the local environment and evaluating the As geochemical budget. The presence of As, and to a certain extent V (Fig. 7c), at concentrations above that of UCC in the berm samples is interpreted as a winnowing effect where denser Fe-oxides and ferromagnesian minerals may be preferentially accumulating as winds mobilize less dense minerals (e.g., quartz). The interpretation of this winnowing effect on the berm sample mineralogy and chemistry is further supported by the observed higher concentrations of Zr, U, and REEs (Table 1), which are consistent with high-density phases such as zircon and REE-phosphates. At present, the exact form(s) of As in all sand samples are not known. It is therefore unknown if As is geochemically mobile in this environment. If mobile, there exists the potential for As release and exposure if sands experience variable redox conditions. No appreciable concentrations of critical minerals or critical metals (e.g., REEs) were observed in the GOL sands. Given the concentrations of critical elements observed, even secondary or tertiary concentrations of Fe-oxide (or ferromagnesian minerals) would likely not be of interest for any critical mineral production. This is consistent with the results of a recent USGS report (2022) which identified 445 "focus areas" within the United States as potential domestic sources of 13 critical minerals. One of these was in Puerto Rico, specifically in the southwestern region of the island.

In the context of hydrogeologic properties, the K values (1.16 cm/s for dune sands, 1.07 cm/s for berm sands, and 1.49 cm/s for shoreface sands) are comparatively high compared to that expected for the grain size distributions (up to 1.49 cm/s; see also; Fetter 2018; Das 2000). This difference is in part explained by the irregular subangular grain shapes observed amongst geogenic grains (e.g., quartz and feldspars; Fig. 4), combined with the internal porosity of biogenic grains and the angularity and irregular surface morphology (Fig. 5). These geotechnical constraints may be of use for addressing future pollution challenges.

Providing detailed characterization of sands that dominate Puerto Rico's coastal environments could aid in future remote sensing investigations of pollution sources and environmental disasters (see also, Krekeler et al. 2023). For example, Allen and Krekeler (2010) demonstrated the utility of reflective spectroscopy through the investigation of numerous petroleum-geogenic substrate combinations to support hyperspectral remote sensing of petroleum spills. Furthermore, Brum et al., (2020) investigated the reflective spectra of gasoline, diesel, and jet fuel-A on sand materials under a range of temperatures. For Puerto Rico and the Caribbean region, significant environmental risk exists

due to the frequency of hurricane, earthquake, tsunami, and landslide events (e.g., Ventura-Valentín and Brudzinski, 2022; Lin et al. 2020; Kwasinski et al. 2019; Manaker et al. 2008; Boose et al. 2004; Dillon et al. 1999; Larsen and Torres-Sánchez 1998; Basnet et al. 1992; Scatena and Larsen 1991). Given these regional hazards, investigations of coastal sands from across Puerto Rico could further support future environmental and remote sensing studies (e.g., Pérez Valentín and Müller 2020) by facilitating the more robust identification and characterization of target materials in the environment.

Conclusions

This study provides a comprehensive mineralogical and geochemical investigation of sands from Playa las Golondrinas in northern Puerto Rico. The datasets provided here contribute to defining an environmental (geogenic) background for the local region and demonstrate the utility of sand as a medium from which a geochemical reference framework can be derived. Sands sampled from the dune, berm, and shore environments are characterized by a unimodal grain size and dominated by quartz, plagioclase feldspar, and lithic clasts as confirmed by microscopy (PLM and SEM), powder XRD, and reflective spectroscopy. Bulk element concentrations from all three coastal environments are consistent with derivation from arc-related rocks in Puerto Rico's interior (i.e., LILE enrichment, Pb-enrichment, and associated Nb–Ta depletion). The majority of bulk elemental concentrations are below that of Earth's average upper continental crust and element Mco-variation trends are interpreted as geogenic, not anthropogenic, in origin. Particularly, berm sands are consistently enriched in Fe, Mn, Ni, Cr, V, and As compared to dune and shoreface environments. This enrichment is interpreted to reflect a wind-related winnowing effect in the coastal environment where denser Fe-oxide phases accumulate. Within the context of potential elements of environmental concern (e.g., Cu, Zn, Pb), no discrete anthropogenic metal-bearing phases or particles were observed.

Results from this investigation provide bulk material property constraints that have the potential to aid in more accurate interpretations of current and future remote sensing imagery. This could help support decision-making related to environmental conservation and emergency management throughout the region. This new mineralogical and geochemical dataset also provides local and regional context for metal pollution, particularly given the ongoing impact of industry and coal pollution in Puerto Rico.

Supplementary Information The online version contains supplementary material available at https://doi.org/10.1007/s12665-024-12010-5.

Acknowledgements Audrey Allen and Maddy Zimmerer were mentored and offered professional development opportunities through an NSF GEOPATHS-EXTRA award (#1801424) to Dr. Claire McLeod (PI) and Dr. Mark Krekeler (Co-PI). No financial support from NSF award #1801424 was provided for research expenses. Audrey Allen and Maddy Zimmerer also completed this work as part of a summer NSF REU grant # DBI-2150197 which supported some research expenses. Spectroradiometry equipment used for this project was acquired through NIJ Forensic Science R&D award 2015-DN-BX-K011 to Dr. Krekeler. We thank Mr. Matt Duley for general assistance. We acknowledge the support of the staff and resources from the Center for Advanced Microscopy and Imaging (CAMI) at Miami University. Spencer Snell was supported by Miami University graduate student summer research funding during this project. Wilnelly Ventura-Valentín, J Abigale O'Connor, and Spencer Snell were supported on Miami University graduate assistantships during the preparation of the manuscript.

Author contributions This project involved undergraduate and graduate students across career stages to maximize educational training and develop skill sets. This required significant support from a post-doc (author Velázquez Santana), staff (author Lytle), and faculty (authors McLeod and Krekeler). Audrey Allen contributed to grain size analysis, carried out initial light microscopy work, collected powder X-ray diffraction data, completed hydraulic conductivity determination work, and sample preparation. Allen also interpreted data and contributed to writing, editing, and figure preparation. Claire McLeod significantly contributed to writing, editing, discussion, data curation, figure design, and analysis of ICP-MS data. Maddy Zimmerer contributed to grain size analysis, carried out initial light microscopy work, collected powder X-ray diffraction data, did hydraulic conductivity determination work, and sample preparation. Will Amick contributed to grain size analysis, reflective spectroscopy, and sample preparation. Ethan Krekeler contributed to sample collection, field safety and logistics, grain size analysis, reflective spectroscopy, hydraulic conductivity determination, and sample preparation. Jonathan Tegge contributed to grain size analysis, sample preparation, and hydraulic conductivity. Liannie Velázquez Santana co-supervised fieldwork, contributed significantly to field logistics and travel efforts, and contributed to sample collection, writing, references, and bibliographic development. Liannie also contributed to writing and editing. Wilnelly Ventura-Valentín, co-supervised fieldwork, contributed significantly to field logistics and travel efforts, sample collection, references, and bibliographic development. Jordan Vest contributed to the collection of samples, field safety, logistics, references, and bibliographic development and editing. Abigale O'Connor contributed to the collection of samples, field safety and logistics, references, and bibliographic development and editing. Marion Lytle supervised students in preparing ICP-MS solutions, trained students in the operation of the powder X-ray diffractometer, and assisted in writing and editing. Landon Stitle contributed significantly to light microscopy data collection, figure preparation, and writing and editing for light microscopy. Barry Shaulis collected and processed ICP-MS solution data and contributed to writing and editing the ICP-MS text. Spencer Snell acquired SEM data for the project and assisted with data management. Mark P. S. Krekeler managed the project, co-supervised fieldwork and safety, managed and coordinated data collection, and contributed to writing and editing.

Funding NSF, NSF GEOPATHS-EXTRA award (#1801424), NSF GEOPATHS-EXTRA award (#1801424), NSF REU grant #

DBI-2150197, NSF GEOPATHS-EXTRA award (#1801424), NSF GEOPATHS-EXTRA award (#1801424), NIJ,Forensic Science R& D award 2015-DN-BX-K011.

Data availability No datasets were generated or analysed during the current study.

Declarations

Conflict of interests The authors declare no competing interests.

References

AAPG (1978) Color guide to petrography of carbonate rocks memoir 77

Allen CS, Krekeler MPS (2010) Reflectance spectra of crude oils and refined petroleum products on a variety of common substrates. SPIE 2010 7687:162–174

Allen A, Dietrich M, McLeod CL, Gillis M, Gokey K, Fouh M, Krekeler MPS (2024) Investigating mercury in road sediment in Michigan City, Indiana: A new type of environmental pollution record. Environ Adv 15:100483. https://doi.org/10.1016/j.envadv.2024.100483

Anderson M, Wanless VD, Perfit M, Conrad E, Gregg P, Fornari D, Ridley WI (2021) Extreme heterogeneity in mid-ocean ridge mantle revealed in lavas from the 8° 20′ N near-axis seamount chain. Geochem Geophy Geosy 22:e2020GC009322

Apeti DA, Whitall DR, Pait AS, Dieppa A, Zitello AG, Lauenstein GG (2012) Characterization of land-based sources of pollution in Jobos Bay, Puerto Rico: status of heavy metal concentration in bed sediment. Environ Monit Assess 184:811–830. https://doi.org/10.1007/s10661-011-2003-0

Argyilan EP, Avis PG, Krekeler MPS, Morris CC (2015) The origin of collapse features appearing in a migrating parabolic dune along the southern coast of Lake Michigan. Aeolian Res 19:137–149. https://doi.org/10.1016/j.aeolia.2015.09.008

Barnes M, McLeod C, Faraci O, Chappell C, Krekeler MPS (2020) Characterizing the geogenic background of the Midwest: A detailed mineralogical and geochemical investigation of a glacial till in southwestern Ohio. Environ Earth Sci 79:159

Barnes SJ, Yao ZS, Mao YJ, Jesus AP, Yang S, Taranovic V, Maier WD (2023) Nickel in olivine as an exploration indicator for magmatic Ni-Cu sulfide deposits: A data review and re-evaluation. Am Mineral 108:1–17. https://doi.org/10.2138/am-2022-8327

Basnet K, Likens GE, Scatena FN, Lugo AE (1992) Hurricane Hugo: damage to a tropical rain forest in Puerto Rico. J Trop Ecol 8:47–55. https://doi.org/10.1017/S0266467400006076

Blott SJ, Pye K (2001) GRADISTAT: A grain size distribution and statistics package for the analysis of unconsolidated sediments. Earth Surf Proc Land 26:1237–1248. https://doi.org/10.1002/esp.261

Boose ER, Serrano MI, Foster DR (2004) Landscape and regional impacts of hurricanes in Puerto Rico. Ecol Mono 74:335–352

Brown P, Vega CMV, Murphy CB, Welton M, Torres H, Rosario Z, Meeker JD (2018) Hurricanes and the environmental justice island: Irma and Maria in Puerto Rico. Environ Just 11:148–153

Brum J, Schlegel C, Chappell C, Burke M, Krekeler MPS (2020) Reflective spectra of gasoline, diesel and jet fuel ion sand substrates under ambient and cold conditions: Implications for detection using hyperspectral remote sensing and development of age estimation models. Environ Earth Sci 79:463. https://doi.org/10.1007/s12665-020-09165-2

Burke M, Rakovan J, Krekeler MPS (2017) A study by electron microscopy of gold and associated minerals from Round Mountain, Nevada. Ore Geol Rev 91:708–717

Burke M, Dawson C, Allen CS, Brum J, Roberts J, Krekeler PS (2019) Reflective spectroscopy investigations of clothing items to support law enforcement, search and rescue, and war crime investigations. Forensic Sci Int 304:109945. https://doi.org/10.1016/j.forsciint.2019.109945

Carlson KM, Asner GP, Hughes RF, Ostertag R, Martin RE (2007) Hyperspectral remote sensing of canopy biodiversity in Hawaiian lowland rainforests. Ecosystems 10:536–549. https://doi.org/10.1007/s10021-007-9041-z

Chen, PY (1977) Table of Key Lines in X-ray Powder Diffraction Patterns of Minerals in Clays and Associated Rocks. Indiana Department of Natural Resources Geological Survey Occasional Paper 21.

Cloutis EA (1989) Spectral reflectance properties of hydrocarbons: remote-sensing implications. Science 245:165–168. https://doi.org/10.1126/science.245.4914.165

Curran PJ (1989) Remote sensing of foliar chemistry. Remote Sens Environ 30:271–278

Curran PJ, Dungan JL, Gholz HL (1990) Exploring the relationship between reflectance red edge and chlorophyll content in slash pine. Tree Physiol 7:33–48. https://doi.org/10.1093/treephys/7.1-2-3-4.33

Curtis J, Stitle L, Certain J, Murchland M, Piszel C, Vest J, McLeod CL, Krekeler MPS (2023) A reflective spectroscopy and mineralogical investigation of cosmetic blush (Wet'N'Wild) potentially for forensic investigations related to interpersonal violence—an experimental feasibility study. Forensic Sci 3:544–559. https://doi.org/10.3390/forensicsci3040038

Cymes BA, Almquist C, Krekeler MPS (2020) Europium-doped cryptomelane: Multi-pathway synthesis, characterization, and evaluation for the gas phase catalytic oxidation of ethanol. Appl Cat A Gen 589:117310. https://doi.org/10.1016/j.apcata.2019.117310

Das BM (2000) Fundamentals of Geotechnical Engineering. Brooks/Cole. 593 p

Dickinson WR (1985) Interpreting provenance relations from detrital modes of sandstones. In: Zuffa GG (ed) Provenance of Arenites. Springer Netherlands, Dordrecht, pp 333–361

Dietrich M, Huling J, Krekeler MPS (2018) Metal pollution investigation of Goldman Park, Middletown Ohio: Evidence for steel and coal pollution in a high child use setting. Sci Tot Environ 618:1350–1362. https://doi.org/10.1016/j.scitotenv.2017.09.246

Dietrich M, Wolfe A, Burke M, Krekeler MPS (2019) The first pollution investigation of road sediment in Gary, Indiana: Anthropogenic metals and possible health implications for a socioeconomically disadvantaged area. Environ Int 128:175–192. https://doi.org/10.1016/j.envint.2019.04.042

Dillon W, Ten Brink U, Frankel A, Mueller C, Rodriguez R (1999) Seismic and tsunami hazards in northeast Caribbean addressed at meeting. Eos 80:309–310

Dung TTT, Cappuyns V, Swennen R, Phung NK (2013) From geochemical background determination to pollution assessment of heavy metals in sediments and soils. Rev Environ Sci Bio/Technol 12:335–353. https://doi.org/10.1007/s11157-013-9315-1

Epting S (2015) The limits of environmental remediation protocols for environmental justice cases: lessons from Vieques, Puerto Rico. Contemp Just Rev 18:352–365. https://doi.org/10.1080/10282580.2015.1057705

Fetter CW (2018) Applied hydrogeology. Waveland Press

Flett L, McLeod C, McCarty J, Shaulis B, Fain JJ, Krekeler MPS (2021) Providing environmental health contexts for Native American populations on the Spokane Reservation, WA: Insights from tree bark particulate matter surrounding the Midnite Uranium Mine. Environ Res 194:110619. https://doi.org/10.1016/j.envres.2020.110619

García-Casco A, Iturralde-Vinent MA, Pindell J (2008) Latest Cretaceous collision/accretion between the Caribbean plate and Caribbean: Origin of metamorphic terranes in the Greater Antilles. Int Geol Rev 50:781–809

Garzanti E (2019) Petrographic classification of sand and sandstone. Earth-Science Rev 192:545–563. https://doi.org/10.1016/j.earscirev.2018.12.014

Garzanti E, Vermeesch P, Andò S, Vezzoli G, Valagussa M, Allen K, Al-Juboury AI (2013) Provenance and recycling of Arabian desert sand. Earth-Sci Rev 120:1–19

Giménez J, Martínez M, de Pablo J, Rovira M, Duro L (2007) Arsenic sorption onto natural hematite, magnetite, and goethite. J Haz Mater 141:575–580

González-Guzmán R, Inguaggiato C, Brusca L, González-Acevedo ZI, Bernard-Romero R (2022) Assessment of potentially toxic elements (PTEs) sources on soils surrounding a fossil fuel power plant in a semi-arid/arid environment: A case study from the Sonoran Desert. Appl Geochem 136:105158. https://doi.org/10.1016/j.apgeochem.2021.105158

Heggie TW, Amundson ME (2009) Dead men walking: search and rescue in US National Parks. Wild Environ Med 20:244–249

Heggie TW, Heggie TM (2009) Search and rescue trends associated with recreational travel in US national parks. J Travel Med 16:23–27. https://doi.org/10.1111/j.1708-8305.2008.00269.x

Hu HY, Stern RJ, Rojas-Agramonte Y, García-Casco A (2022) Review of geochronologic and geochemical data of the Greater Antilles Volcanic Arc and implications for the evolution o f oceanic arcs. Geochem Geophy Geosy 23:e2021GC010148

Hunt GR (1977) Spectral signatures of particulate minerals in the visible and near infrared. Geophysics 42:501–513

Hunt GR, Logan LM (1972) Variation of single particle mid-infrared emission spectrum with particle size. Appl Optics 11:142–147. https://doi.org/10.1364/AO.11.000142

Hunt GR, Salisbury JW, Lenhoff CJ (1971a) Visible and near-Infrared Spectra of Minerals and Rocks III: Oxides and Hydroxides. Modern Geol 2:195–205

Hunt GR, Salisbury JW, Lenhoff CJ (1971b) Visible and near-Infrared Spectra of Minerals and Rocks IV: Sulphides and Sulphates. Modern Geol 3:1–14

Hunt GR, Salisbury JW, Lenhoff CJ (1973) Visible and near-infrared spectra of minerals and rocks VI: additional silicates. Modern Geol 4:85–106

Jiang J, Wang J, Liu S, Lin C, He M, Liu X (2013) Background, baseline, normalization, and contamination of heavy metals in the Liao River Watershed sediments of China. J Asian Earth Sci 73:87–94

Jollands MC, Dohmen R, Padrón-Navarta JA (2023) Hide and seek—trace element incorporation and diffusion in olivine. Elements 19:144–150

Kelley KA, Plank T, Ludden J, Staudigel H (2003) Composition of altered oceanic crust at ODP Sites 801 and 1149. Geochem Geophy Geosy 4:8910. https://doi.org/10.1029/2002GC000435

Klein E, Krekeler MPS (2020) The occurrence of Hg, Se, S, Ni, Cr, and Th in talc ore: A scanning electron microscopy (SEM) study of historical samples from the Willow Creek mine. Montana. Results Geochem 1:100003

Kolker A, Nordstrom DK (2001) Occurrence and micro-distribution of arsenic in pyrite. US Geol Surv website. http://wwwbrr.cr.usgs.gov/Arsenic/

Krekeler MP, Allen CS (2008) Remote sensing spectra of cesium chloride provides a potential emergency management tool for response to a radiological dispersal device detonation. J Emerg Manage 6:60–64

Krekeler MPS, Burke M, Allen S, Sather B, Chappell C, McLeod CL, Loertscher C, Loertscher S, Dawson C, Brum J, Fackey D (2023) A novel hyperspectral remote sensing tool for detecting and analyzing human materials in the environment: a geoenvironmental approach to aid in emergency response. Environ Earth Sci 82:109

Kuisma-Kursula P (2000) Accuracy, precision and detection limits of SEM–WDS, SEM–EDS and PIXE in the multi-elemental analysis of medieval glass. X-Ray Spectro Int J 29:111–118

Kwasinski A, Andrade F, Castro-Sitiriche MJ, O'Neill-Carrillo E (2019) Hurricane Maria effects on Puerto Rico electric power infrastructure. IEEE Pow Energ Technol Sys J 6:85–94

Lakshmipathiraj P, Narasimhan BRV, Prabhakar S, Raju GB (2006) Adsorption of arsenate on synthetic goethite from aqueous solutions. J Haz Mater 136:281–287

Larsen MC, Torres-Sánchez AJ (1998) The frequency and distribution of recent landslides in three montane tropical regions of Puerto Rico. Geomorphology 24:309–331. https://doi.org/10.1016/S0169-555X(98)00023-3

Leblanc G, Francis CM, Soffer R, Kalacska M, de Gea J (2016) Spectral reflectance of polar bear and other large arctic mammal pelts; potential applications to remote sensing surveys. Remote Sens 8:273

Lin Y, Sevillano-Rivera M, Jiang T, Li G, Cotto I, Vosloo S, Carpenter CMG, Larese-Casanova P, Giese RW, Helbling DE, Padilla IY, Rosario-Pabón Z, Vélez Vega C, Cordero JF, Alshawabkeh AN, Pinto A, Gu AZ (2020) Impact of Hurricane Maria on drinking water quality in Puerto Rico. Environ Sci Technol 54:9495

Lindeman C, Oglesbee T, McLeod C, Krekeler MPS (2020) Mineralogy and geochemistry of theKinnikinic Quartzite at the Arco Hills Silica and Gold Project in Butte County, Idaho: Results of an ore quality spot check and implications for potential plasma furnace processing. Minerals 10:523. https://doi.org/10.3390/min10060523

Lirong Y, Ning Z, Leping Y, Huaijun G (2017) Distribution of U-Pb ages of detrital zircon from the Hobq Desert and its implications for provenance. Quat Sci 37:560–569

Lloréns H, Santiago R (2018) Women Lead Puerto Rico's Recovery. In Puerto Rico's southeast, women are at the forefront of the struggle against environmental degradation and catastrophe. NACLA Rep Am 50:398–403. https://doi.org/10.1080/10714839.2018.1550985

Lytle ML, Kelley KA, Hauri EH, Gill JB, Papia D, Arculus RJ (2012) Tracing mantle sources and Samoan influence in the northwestern Lau back-arc basin. Geochem Geophy Geosy 13:Q10019. https://doi.org/10.1029/2012GC004233

Mamindy-Pajany Y, Hurel C, Marmier N, Roméo M (2009) Arsenic adsorption onto hematite and goethite. C R Chim 12:876–881

Manaker DM, Calais E, Freed AM, Ali ST, Przybylski P, Mattioli G, Jansma P, Prépetit C, De Chabalier JB (2008) Interseismic plate coupling and strain partitioning in the northeastern Caribbean. Geophy J Int 174:889–903. https://doi.org/10.1111/j.1365-246X.2008.03819.x

Mango H, Ryan P (2015) Source of arsenic-bearing pyrite in southwestern Vermont, USA: sulfur isotope evidence. Sci Tot Environ 505:1331–1339

Matsitsi SM, Linturi JM, Kebwaro JM, Maweu OM (2019) Effects of Seasonal Change on the Levels of Geogenic Radionuclides in Sand and Rocks from Tyaa River deposit in Kitui County. Int J Fund Phys Sci 9:14–19

McCaffrey KT (2018) Environmental remediation and its discontents: the contested cleanup of Vieques, Puerto Rico. J Polit Ecol 25:80–103

Meinecke III L (1972) A geochemical reconnaissance of Puerto Rican beach sands. [M.S. Thesis University of Missouri-Rolla] https://scholarsmine.mst.edu/cgi/viewcontent.cgi?article=5187&context=masters_theses

Monroe WH (1968) The Aguada Limestone of northwestern Puerto Rico Geological Survey Bulletin USGS. https://pubs.usgs.gov/bul/1274g/report.pdf

Nesse W (2013) Introduction to Optical Mineralogy. Oxford University Press 348p

O'Shea M, Krekeler MPS, Vann DR, Gieré R (2021) Investigation of Pb-contaminated soil and road dust in a polluted area of Philadelphia. Environ Monit Assess 193:440. https://doi.org/10.1007/s10661-021-09213

Oglesbee T, McLeod C, Chappell C, Vest J, Sturmer D, Krekeler MPS (2020) A Mineralogical and Geochemical Investigation of Modern Aeolian Sands near Tonopah, Nevada: Sources and Environmental Implications. CATENA 194:104640

Pastore G, Baird T, Vermeesch P, Bristow C, Resentini A, Garzanti E (2021) Provenance and recycling of Sahara Desert sand. Earth-Science Rev 216:103606. https://doi.org/10.1016/j.earscirev.2021.103606

Paul KC, Silverstein J, Krekeler MPS (2017) New insights into rare earth element particulate generated by cigarette lighters: an electron microscopy and materials science investigation of a poorly understood indoor air pollutant and constraints for urban geochemistry. Environ Earth Sci 76:369. https://doi.org/10.1007/s12665-017-6687-5

Pérez Valentín JM, Müller MF (2020) Impact of Hurricane Maria on beach erosion in Puerto Rico: Remote sensing and causal inference. Geophy. Res Let 47:e2020GL087306

Pérez-Alvelo KM, Llegus EM, Forestier-Babilonia JM, Elías-Arroyo CV, Pagán-Malavé KN, Bird-Rivera GJ, Rodríguez-Sierra CJ (2021) Microplastic pollution on sandy beaches of Puerto Rico. Mar Poll Bull 164:112010. https://doi.org/10.1016/j.marpolbul.2021.112010

Pettijohn FJ, Potter PE, Siever R (2012) Sand and sandstone. Springer Sci Business Media. https://doi.org/10.1007/978-1-4612-1066-5

Qiu G, Gao T, Hong J, Tan W, Liu F, Zheng L (2017) Mechanisms of arsenic-containing pyrite oxidation by aqueous arsenate under anoxic conditions. Geochim Cosmochim Acta 217:306–319

Ramos JP, Mann P (2023) Late Cretaceous-Recent tectonostratigraphic evolution of the Yucatan back-arc basin, northern Caribbean sea. Geochem Geophy Geosy 24:e2023GC010933

Rodríguez-Martínez EM, Pérez EX, Schadt CW, Zhou J, Massol-Deyá AA (2006) Microbial diversity and bioremediation of a hydrocarbon-contaminated aquifer (Vega Baja, Puerto Rico). Int J Env Res Pub Health 3:292–300. https://doi.org/10.3390/ijerph2006030036

Rudnick RL, Gao S (2003) Composition of the Continental Crust. Treatise on Geochemistry, 3, (eds), Holland, H.D, Turekian, K.K, pp. 659, p. 1–64

Sánchez-Colón YM, Schaffner FC (2021) Identifying nonpoint sources of phosphorus and nitrogen: a case study of pollution that enters a freshwater wetland (Laguna Cartagena, Puerto Rico). J Water Resource Protect 13:588–604

Sánchez-Colón YM, Chévere-Del Río JA, Sánchez-Guzmán NM, Schaffner FC (2022) An assessment of water quality parameters at the Cerrillos Reservoir, Ponce, Puerto Rico in the aftermath of Hurricane Maria. J Water Resour Prot 14:35–49. https://doi.org/10.4236/jwarp.2022.141003

Scatena FN, Larsen MC (1991) Physical aspects of hurricane Hugo in Puerto Rico. Biotropica 23:317–323. https://doi.org/10.2307/2388247

Schoneveld L, Barnes SJ, Makkonen HV, Le Vaillant M, Paterson DJ, Taranovic V, Wang KY, Mao YJ (2020) Zoned pyroxenes as prospectivity indicators for magmatic Ni-Cu sulfide mineralization. Front Earth Sci 8:256

Skanavis C (1999) Groundwater Disaster in Puerto Rico: The Need for Environmental Education. J Environ Health 62:29

Smith JV (2012). Feldspar minerals: 2 chemical and textural properties. Springer Science & Business Media

Strekeisen A (2020) Gastropods (Class Gasteropoda) (Cambrian – Present) alexstrekeisenit https://wwwalexstrekeisenit/english/sedi/gastropodsphp

Sturm P, Viqueira R, Ferguson R, Moore T (2012) Addressing land-based sources of pollution in Guánica, Puerto Rico. In Proceedings of the 12th International Coral Reef Symposium, Cairns, Australia (pp. 9–13)

Sun SS, McDonough WF (1989) Chemical and isotopic systematics of oceanic basalts: implications for mantle composition and processes. Geological Society, London, Special Publications 42:313–345

Tomic T, Schmid K, Lutz P, Domel A, Kassecker M, Mair E, Grixa IL, Ruess F, Suppa M, Burschka D (2012) Toward a fully autonomous UAV: Research platform for indoor and outdoor urban search and rescue. IEEE Rob Auto Mag 19:46–56

USGS (1957) A reconnaissance study of the Beach Sands of Puerto Rico. Geological Survey Bulletin 1942-I. https://pubs.usgs.gov/bul/1042i/report.pdf

USGS (2022) Focus areas for data acquisition for potential domestic resources of 13 critical minerals in the conterminous United States and Puerto Rico—Antimony, barite, beryllium, chromium, fluorspar, hafnium, helium, magnesium, manganese, potash, uranium, vanadium, and zirconium. Report 2019–1023-D. https://doi.org/10.3133/ofr20191023D

Ustin SL, DiPietro D, Olmstead K, Underwood E, Scheer GJ (2002) Hyperspectral remote sensing for invasive species detection and mapping. In Geoscience and Remote Sensing Symposium 2002. IGARSS'02.2002 IEEE Int 3:1658–1660

Vandeuren A, Pereira B, Kaba AJ, Titeux H, Delmelle P (2023) Environmental bioavailability of arsenic, nickel and chromium in soils impacted by high geogenic and anthropogenic background contents. Sci Tot Environ 902:166073. https://doi.org/10.1016/j.scitotenv.2023.166073

Velázquez Santana LV, McLeod CL, Blakemore D, Shaulis B, Hill T (2020) Bolivian hornblendite cumulates: Insights into the depths of Central Andean arc magmatic systems. Lithos 370:105618. https://doi.org/10.1016/j.lithos.2020.105618

Ventura-Valentín W, Brudzinski MR (2022) Characterization of swarm and mainshock–aftershock behavior in Puerto Rico. Seismol Soc Am 93:641–652. https://doi.org/10.1785/0220210329

Wu S, Heberling MT (2013) The distribution of pollution and environmental justice in Puerto Rico: a quantitative analysis. Pop Environ 35:113–132

Wudke H, Brown K, Murchland M, Gillis M, Gokey K, Bank J, Lytle M, McLeod CL, KrekelerMPS, (2024) Mineralogical and geochemical characterization of Johnson's baby powderfrom 1985:

Evidence of contamination. Appl Clay Sci 250:107252. https://doi.org/10.1016/j.clay.2023.107252